Article type: Full Paper

Graphitic-Based Solid-State Supercapacitors: Enabling Redox Reaction by In-Situ Electrochemical Treatment

Mojtaba Amjadipour[1], Dawei Su[2, 3], and Francesca Iacopi[1, 3]*

[1] Dr. Mojtaba Amjadipour and Prof. Francesca Iacopi. School of Electrical and Data Engineering, Faculty of Engineering and Information Technology, University of Technology Sydney, NSW, Australia.

[2] Dr. Dawei Su. School of Mathematical and Physical Sciences, Faculty of Science, University of Technology Sydney, NSW, Australia.

[3] Dr. Dawei Su and Prof. Francesca Iacopi. Centre for Clean Energy Technology, University of Technology Sydney, NSW, Australia.

Keywords

Quasi-solid-state supercapacitors, graphitic carbon, electrode functionalization, PVA electrolyte

Abstract

The quest for supercapacitors that can hold both high energy and power density is of increasing significance as the need for green and reliable energy storage devices grows, for both large-scale and integrated systems. While supercapacitors for integrated technologies require a solid-state approach, gel-based electrolytes are generally not as efficient as their aqueous counterparts. Here we demonstrate a strategy to enhance the performance of quasi-solid-state supercapacitors made by graphitized silicon carbide on silicon electrodes and polyvinyl alcohol (PVA) + H_2SO_4 gel electrolyte. The electrochemical characterization shows an increase of the specific capacitance of

the cell up to 3-fold resulting from a simple agent-free, in-situ, electrochemical treatment leading to functionalization of the graphitic electrodes. The functionalization of the electrodes simultaneously enables redox reactions, without adding any redox agent, and increases the double layer contribution to the overall capacitance. The strategy and insights offered by this work hold great promise for improving quasi-solid-state, miniaturized on-chip energy storage systems, which are compatible with silicon electronics.

1. Introduction

The rapid development of portable and wireless electronics has significantly increased the demand for integrated energy storage devices. Additionally, the emerging need for clean energy sources such as solar and wind energies further increases the demand for reliable and maintenance-free batteries and supercapacitors [1-2]. Electrochemical supercapacitors have attracted a lot of attention due to their high power density capability as storage devices [3-6]. Their environmentally friendly and long cyclability characteristics make electrochemical supercapacitors prominent candidates for future integrated energy storage devices [2, 7].

The charge storage in the electrochemical supercapacitors is based primarily on electrical double layer capacitance (EDLC), and to a smaller extent, on redox reactions or pseudocapacitance [1, 8]. EDLC relies on ions adsorption at the electrode/electrolyte interface in the presence of an electric field [9]. Redox reactions in supercapacitors store charge via a fast and reversible charge transfer reaction between electrolyte ions and the electrodes [10]. Those reactions are commonly introduced by adding a variety of external redox agents to the system and devising an appropriate functionalization of the electrodes [8, 11-15]. Some widely used redox additives to the electrolyte are P-phenylenediamine, hydroquinone and indigo carmine [16-17]. Overall, the amount,

accessibility and quality of the interfaces between the electrode and electrolyte are critical to the performance of the supercapacitors.

Traditionally, supercapacitors are fabricated using liquid electrolytes, making them prone to undesirable electrolyte leakage issue [4, 18]. The packaging requirements needed to guarantee leakage-free cells makes them too large and unpractical for miniaturized applications. Therefore, gel-based electrolytes are an alternative solution to address this issue [3, 19-20]. The gel electrolytes can potentially also overcome other typical challenges of supercapacitors, such as corrosion, self-discharge, solvent evaporation, and consuming at elevated temperatures [4]. Gel electrolytes are often made of a mixture of a polymer (such as PVA) and an acid (typically H_2SO_4 or H_3PO_4) [1, 21]. PVA-acid based gel electrolytes have not been considered active redox materials. Therefore, the addition of redox agents has been the conventional way to enable the redox contribution in charge storage [11-13]. Moreover, gel electrolytes are generally not as efficient as their aqueous counterparts in terms of charge storage, among others, due to the low charge carrier mobilities [11, 22]. This fundamental limitation prompts the need for more research into mechanisms to enhance the performance of gel electrolytes.

Carbon-based materials such as graphite, graphene oxide, carbon nanotubes, and graphene have been widely explored as electrode materials for supercapacitors [1, 8, 23-26]. Graphene and graphitic carbon-based electrodes have proven to be a very promising choice due to their superior electrical and electrochemical properties, including high surface area and high conductivity [1]. While graphene-based electrodes are a preferred option for flexible devices [1, 23, 27], graphene or graphitic carbon directly fabricated on silicon substrates offer significant potential for on-chip supercapacitors that can be embedded in integrated circuits [8, 28-35]. Among various synthesis methods of graphene/graphitic carbon, a metal-based catalytic synthesis on silicon carbide on

silicon stands out as one of the most versatile and compatible with the current semiconductor industry [30, 36-38]. It offers a binder-free approach to fabricate graphene with high adhesion and tunable characteristics directly on silicon wafers [38]. Also, this approach can be employed for miniaturization and wafer-level fabrication [30, 36-38].

In this work, we demonstrate the possibility of enhancing the performance of quasi-solid-state supercapacitors on silicon using a PVA+H_2SO_4 gel electrolyte through an agent-free, in-situ functionalization of graphitic carbon electrodes. We show that this procedure triggers redox reactions not available with the as-prepared cells, in addition to improving the EDLC charge storage contribution.

2. Results and Discussion

The graphene synthesis on cubic silicon carbide using Ni metal catalyst layers, either alone or alloyed with Cu, provides control over the defect density as well as the porosity of the graphitized electrodes [36, 39]. We investigated and compared three different types of electrodes: low-defect, oxidized and porous graphitic electrodes (refer to the Experimental Section).

Scanning electron microscopy (SEM) and atomic force microscopy (AFM) are used to compare the surface morphology of the different electrode types. Both methods are in agreement, revealing similar surface images. Open pores with dimensions of several microns are clearly visible on the porous electrodes surface (**Figure 1c**, **S2c, 1f**). This porosity stems from a repeated Ni diffusion, intrusion and removal of nickel silicides [39].

The oxidized (**Figure 1b**, **S2b, 1e**) and the low-defect electrodes (**Figure 1a**, **S2a, 1d**) do not show significant porosity on the surface, but they reveal a finer granular pattern that seems to be common across all of the electrode types. This pattern corresponds to particle sizes in the range

of 80-150 nm, which is also confirmed in the power spectral densities (PSD) extracted from the AFM images. Although the PSDs for the different electrodes show very different distributions, all of them show evident peaks at spatial frequencies in the 8-12 μm^{-1} range (**Figure S3**), corresponding to the granularity discussed above. The RMS roughness estimated for the porous electrodes is ~72 nm, which is significantly higher than the low-defect (~25 nm) and the oxidized electrodes (~20 nm). The corresponding AFM height profiles in **Figures 1g, h** and **i**, provide a further comparison of the different surface roughness.

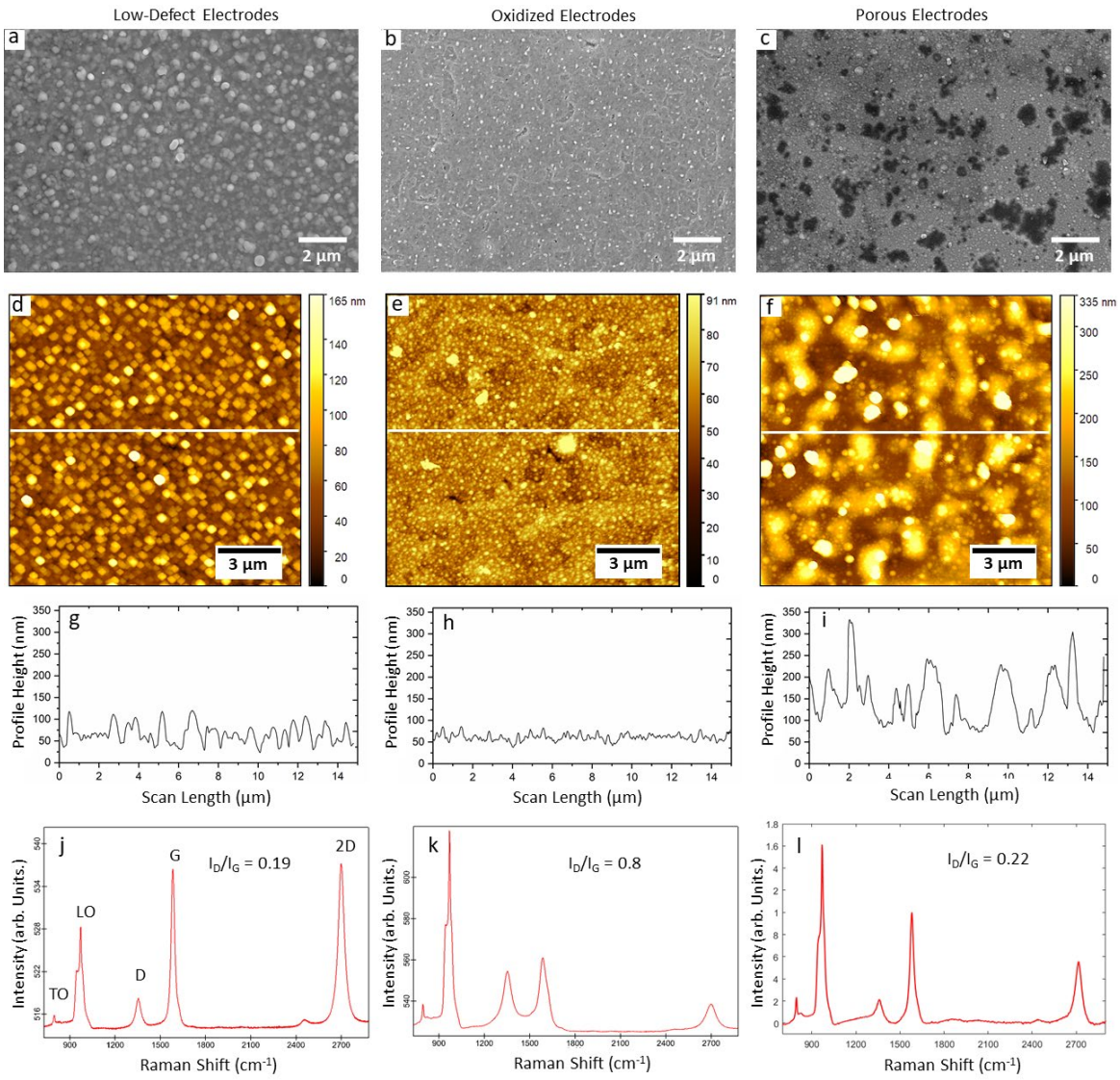

Figure 1. SEM images showing the surface morphology of the different graphitic electrodes: (a) low-defect, fabricated via 10 nm Ni and 20 nm Cu catalytic layers; (b) oxidized, synthesized by using a very thin Ni layer (~3 nm), and (c) porous, fabricated using two rounds of Ni graphitization. AFM images of the (d) low-defect (e) oxidized, and (f) porous graphitic electrodes; the white section lines represent where the height profiles are extracted. Height profiles for the (g) low-defect (h), oxidized, and (i) porous graphitic electrodes. Raman spectra of (j) low-defect (k) oxidized and (l) porous graphitic electrodes. These averaged spectra are collected over 2500 sites over a 100 µm^2 area each.

Raman spectroscopy yields crucial information about the as-prepared graphitized electrodes. Three distinct peaks in the Raman spectrum of graphitic carbon can be assigned to D, G, and 2D bands, respectively [40-41]. The D band is activated by the presence of defects within the graphene lattice, while G and 2D bands are related to the sp^2 bonded carbon lattice [41]. Among other recognizable peaks in the Raman spectra (**Figure 1g-i**) are the TO (at ~850 cm^{-1}) and LO (at ~972 cm^{-1}) silicon carbide peaks, which are related to the 3C-SiC/Si pseudo-substrate [42-43]. The intensity ratio between D and G peaks (I_D/I_G) is commonly used as an indicator for graphene defect density assessment, i.e. higher I_D/I_G ratios indicate a higher defect density [30]. As can be noted from **Figure 1g-i**, the electrode graphitized by depositing Ni and Cu layers has the lowest defect density (**Figure 1g**), while the sample fabricated by a 3 nm Ni layer has the highest defect density (**Figure 1h**). These defects typically also translate into a high amount of oxidization in the graphitic carbon due to a sensibly higher amount of chemically active sites (edges and vacancy defects) available for bonding with oxygen species. The Raman spectra of the defective graphitic electrodes match with previously reported spectra for oxidized graphene [44-45]; therefore, we refer to the highly defective graphitic electrodes as oxidized ones (**Figure 1h**).

Figure 2 shows the cyclic voltammetry (CV) test results of the cells fabricated using the electrodes in a sandwiched configuration (**Figure S1**). The initial CV curve represents a quasi-rectangular shape which is the characteristics of EDLC-based charge storage (**Figure 2a**, **c,** and **e**) [9]. No obvious indications of faradaic reactions are observed from the CV curves related to as-prepared electrodes. The CV tests indicate that the cell fabricated with the oxidized electrodes shows a significantly higher EDLC charge storage performance in the as-prepared condition (larger area of the CV curve). This is expected, as the presence of oxygen species on the

graphitic surface offers more chemically active electrodes, which is desirable for an enhanced EDLC [12].

Therefore, we have devised a strategy to enhance further the cell capacitance through an in-situ electrochemical treatment of the electrodes. By charging the supercapacitor cells with potentials beyond the water decomposition voltage (~1.2 V), we can expect to induce partial electrolysis of the water content in the electrolyte. Charging the cells with 2V, would break water molecules and generate chemically active and mobile species in the electrolyte, able to react in-situ with the graphitic electrodes, particularly at their defective sites. Hence we explore this avenue as a method to functionalize the electrodes electrochemically and in-situ, e.g. creating or enhancing the amount of oxygen-containing functional groups on the electrodes' surface.

We show in **Figure 2** that this in-situ functionalization approach leads in fact to a significant capacitance enhancement. The quasi-rectangular-area components of the CV curves show a substantial increase after the functionalization process, indicating an EDLC enhancement. Simultaneously, two faradaic peaks appear in the CV curves for all 3 types of cells, indicating the triggering of redox reactions (**Figure 2b**, **d** and **f**). The total capacitance enhancement thus results from a combination of an increase of the EDLC component as well as the enablement of redox reactions in the cells. The redox peaks appear in two different regions: at 0.4 – 0.52 V during the charging process and 0.09 – 0.2 V for the discharging process. It should be noted that the redox peaks are here triggered without the addition of external redox agents [11, 18]. Aljafari et al [18] have recently reported that the PVA+H_2SO_4 gel electrolyte can be a redox-active material. However, they had not been able to observe evident faradaic peaks in their CV curves [18].

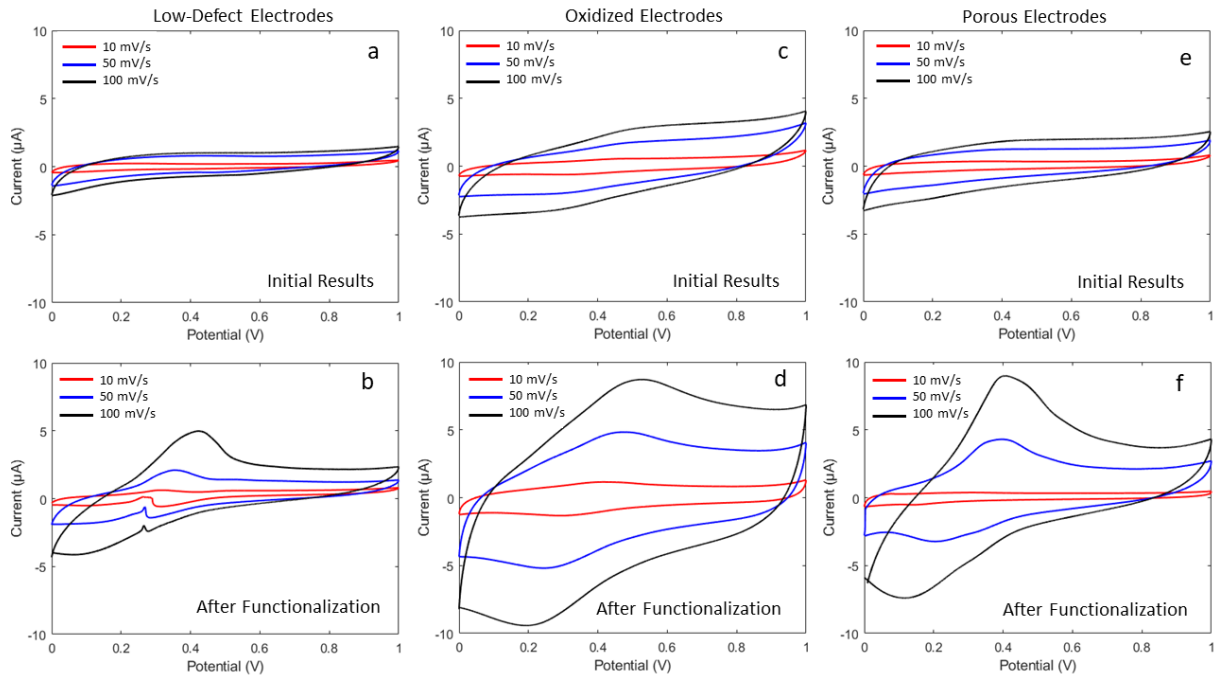

Figure 2. CV curves (a) initial results of cell fabricated by the low-defect graphitic electrodes; (b) after functionalization; (c) initial results of the cell made of the oxidized electrodes; (d) after functionalization; (e) initial results of cell fabricated by porous electrodes; (f) after functionalization, where redox peaks are observed for all 3 types of electrodes/cells.

Figure 3 shows the galvanostatic charge/discharge behavior of the cells. The charge/discharge tests confirm that all cells fabricated with the oxidized electrodes show a significant enhancement of charge storage after functionalization compared to their as-prepared counterparts. In particular, the cell using oxidized electrodes shows an over 3-fold increase in capacitance after charging of the cell at 2V for an in-situ functionalization (see values in **Table 1**). The fact that this type of cell shows the largest extent of enhancement demonstrates that the initial density of chemically active sites (or defects) is a key factor in the efficacy of the in-situ functionalization. In addition to the capacitance enhancement, we observe a significant improvement also in the Coulombic efficiency, particularly for the oxidized electrodes, as indicated by the data in **Table S1**.

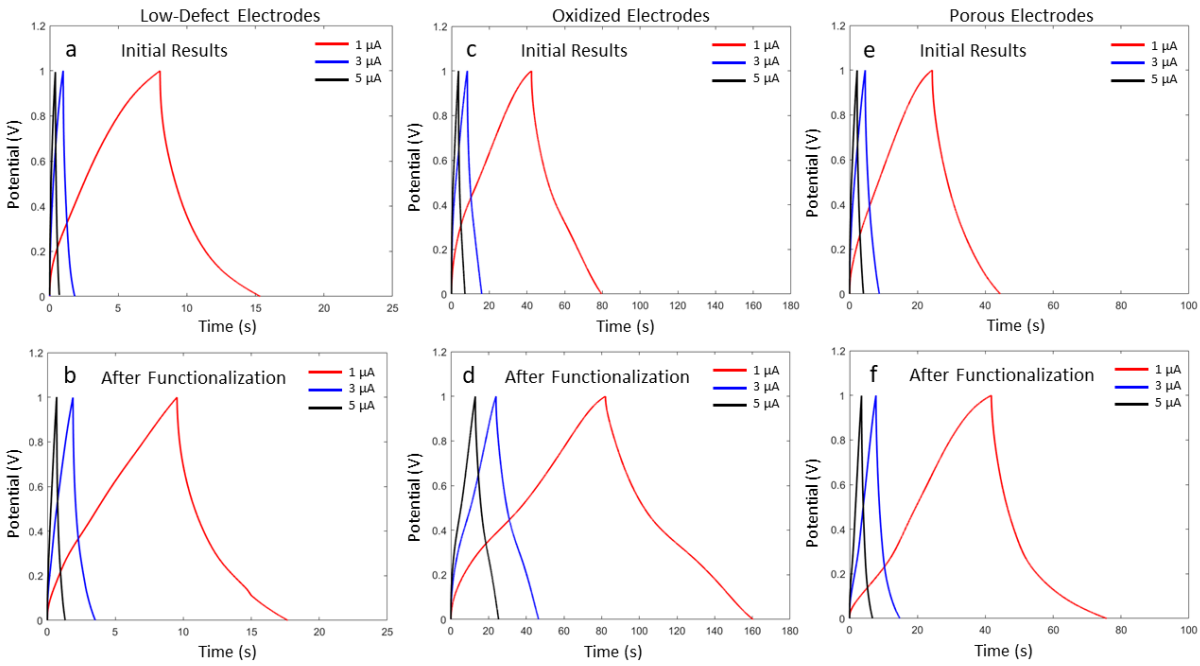

Figure 3. Galvanostatic charge/discharge (a) initial results of cell fabricated with the low-defect graphitic electrodes (b) the same cell after functionalization (c) initial results of cell fabricated with the oxidized electrodes (d) the same cell after functionalization (e) initial results of cell made of the porous electrodes (f) the same cell after functionalization.

Table 1. Quasi-solid-state supercapacitors with different types of graphitic electrodes and their performance calculated from galvanostatic charge/discharge tests. The electrodes' specific capacitance before and after in-situ electrochemical functionalization are compared, showing a substantial improvement after functionalization, particularly for the oxidized electrodes.

Electrode Type	I (µA)	C (µF/cm²)		
		Before functionalization	After functionalization	Improvement (%)
Oxidized	1	110 ± 1%	255 ± 1%	132
	3	62 ± 1%	219 ± 1%	253

	5	43 ± 1%	195 ± 1.5%	342
Porous	1	54 ± 1.5%	70 ± 2%	30
	3	33 ± 1%	44 ± 1%	32
	5	24 ± 1%	35 ± 1%	46
Low-defect	1	16 ± 1%	19 ± 1%	19
	3	6 ± 2%	11 ± 1%	83
	5	4 ± 2%	7 ± 1%	87

The electrochemical impedance spectroscopy was conducted before and after the functionalization process. The Nyquist impedance plots for the cell fabricated with the oxidized electrodes show that the cell resistance has slightly increased after the functionalization (**Figure 4a** and **b**). This resistance increase is in agreement with the functionalization of the graphene electrodes [46]. Although the shapes of the curves are different, both other cell types show a similar increase in transfer impedance after the in-situ functionalization process (**Figure S5**).

Long charge/discharge measurements of the cell fabricated with the oxidized graphitic electrodes after the functionalization process show a reasonably long cyclability, with capacitance retention of ~90% after 6000 cycles (**Figure 4c**). CV test results before and after the long charge/discharge cycling tests still show the presence of the redox contribution, which appears thus to be a consistent contribution to the overall cell capacitance after the functionalization (**Figure 4d**).

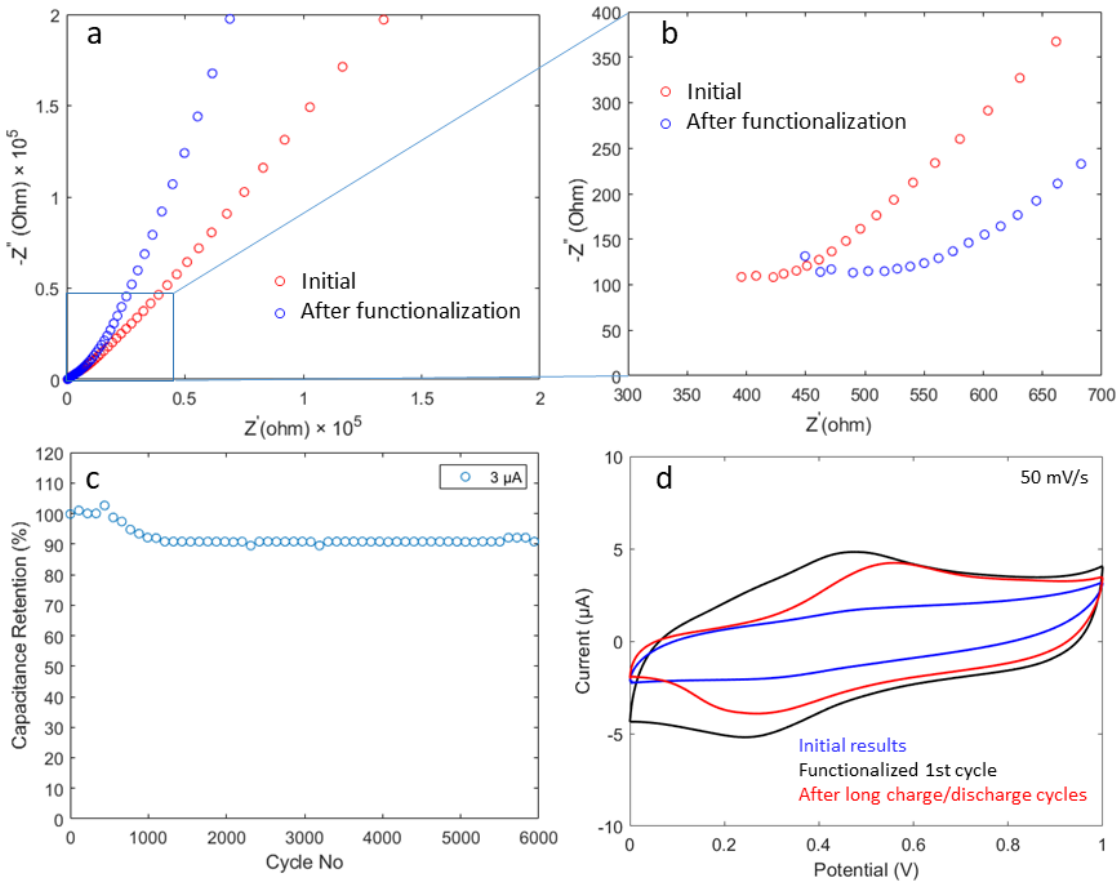

Figure 4. AC Impedance spectroscopy results of the cell fabricated with the oxidized electrodes (a) full spectra and (b) low impedance region. (c) Long cycling charge/discharge test results of the same cell (d) CV curves comparing the cell capacitance with as-prepared electrodes, after in-situ functionalization, and the latter after 6000 charge/discharge cycles, showing still substantially higher capacitance than the cell with as-prepared electrodes.

Figure 5a compares the Raman spectra of the oxidized electrodes before and after the functionalization process - the latter was collected by opening the cell after the in-situ functionalization, measuring through the electrolyte covering the graphitic electrode (inset in **Figure 5a**). While Raman spectroscopy does not show significant changes in the main graphitic peaks (D, G, and 2D), additional observed peaks at ~1435 cm^{-1} and ~2934 cm^{-1} stem from the PVA [47-48]. Joshi et al [47] reported similar spectra for graphene nanoribbons bonded to PVA.

The FTIR spectrum of the as-prepared oxidized electrodes in **Figure 5b** shows peaks related to the 3C-SiC, TO peak at 794 cm^{-1}, LO at 970 cm^{-1}, in addition to a peak around 1060 cm^{-1} which is commonly attributed to the epoxy functional groups and a peak at ~1225 cm^{-1} which originates from the hydroxyl functional groups [49-52]. FTIR spectra of the oxidized electrodes after the in-situ electrochemical treatment confirm the enhanced presence of oxygen functional groups on the surface (**Figure 5b and S7**). A significant intensity increase of the peak around 1060 cm^{-1} after the functionalization process of about 30% supports the enhancement of the oxygen functional groups at the graphitic electrodes' surface. Energy-dispersive X-ray spectroscopy (EDS) measurements also show a sixfold increase in the overall amount of oxygen species after functionalization (**Figure S6**).

In light of all of the information above, we propose a likely mechanism for the enhanced supercapacitor performance. We suggest that charging the supercapacitors with potentials over the water decomposition voltage splits some of the water molecules within the electrolyte, creating free hydroxyl groups, which can then react with the graphitic electrodes' surface forming oxygen-containing groups, including epoxy. The possibility of such surface chemical reactions has been previously supported in the literature [53-54]. Using first-principles calculations, Ghaderi and Peressi [53] have indicated that hydroxyl ions can convert and form epoxy groups on the graphene surface. This mechanism leads to a simple, in-situ preparation of functionalized electrodes, which is the key to triggering redox reactions and enhancing the EDLC performance.

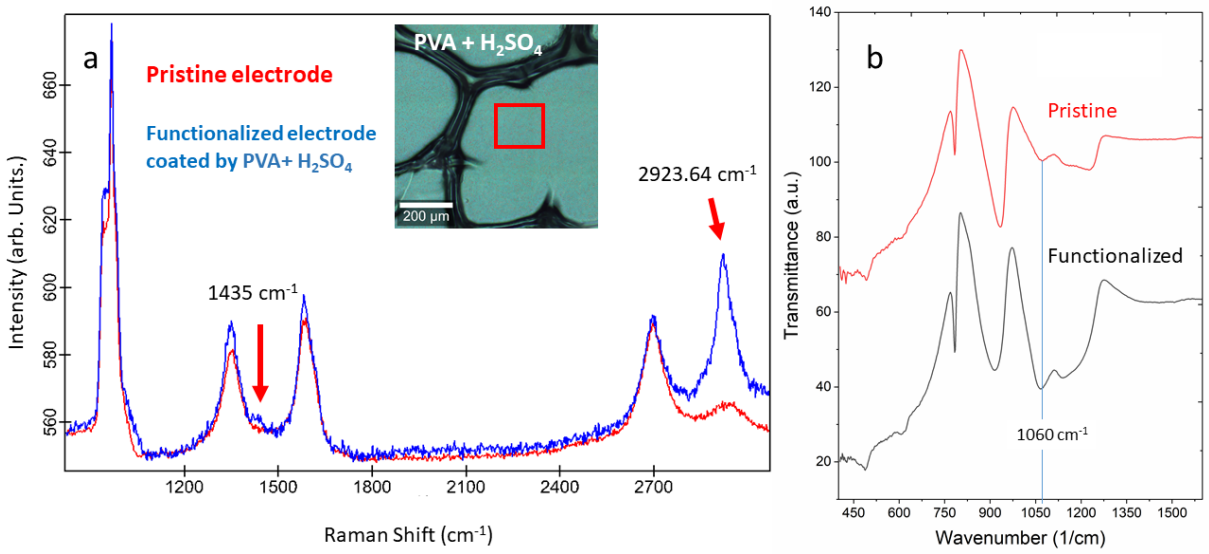

Figure 5. (a) Raman spectra of the oxidized electrodes, inset shows an optical image of the area measured by Raman, and (b) FTIR spectra, before and after the agent-free in-situ functionalization of the oxidized electrodes (electrolyte removed).

In addition, the elevated amount of oxygen functional groups induced on the graphitic surface by the functionalization process is expected to significantly increase the graphene inter-layer spacing, potentially up to ~0.45 nm as we have recently shown [49]. An increased inter-layer spacing, as well as an anticipated improved wettability of the graphitic electrodes due to the functionalization, would enable the PVA molecules to diffuse more efficiently between the electrode layers and intercalate the graphene, overall greatly enhancing the total extent of electrode/electrolyte interface in the cell, hence the EDLC capacitance (see schematic in **Figure 6**). Note that the PVA does not necessarily need to become chemically bonded to the graphitic electrodes for this mechanism to take place. We also note that the Coulombic efficiency improvement is likely a result of the enhanced electrode/electrolyte intercalation, leading likely to shorter ionic transport paths.

These data also show the importance of chemically-active graphitic electrodes in triggering redox reactions using a PVA+H_2SO_4 gel electrolyte [22]. We suggest that the redox reaction at the electrode/electrolyte interface originates from the elevated presence of oxygen functional groups [55]. Although we do not exclude the possibility for additional surface mechanisms, we believe that the most likely redox reaction is the repetitive transformation of the hydroxyl groups to the epoxy groups at the interface ($hydroxyl \leftrightarrow epoxy + 2H^+ + 2e^-$). Also, some redox contribution may arise from the reaction suggested by Aljafari et al [18] through reacting part of the OH branches in the PVA with the H_2SO_4 anions within the volume of the gel electrolyte.

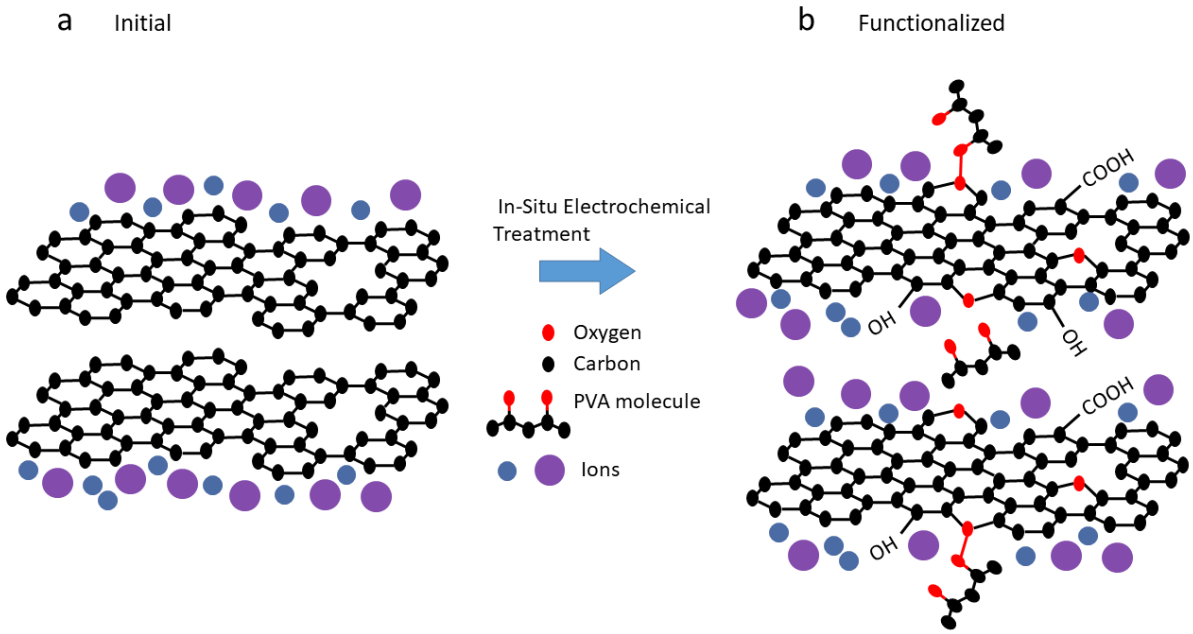

Figure 6. A schematic representation of the agent-free in-situ functionalization mechanism leading to a significant capacitance improvement; (a) as-prepared electrodes (b) electrodes after the functionalization.

3. Conclusions

In summary, we have demonstrated a methodology to enable stable redox reactions in PVA-H_2SO_4 gel electrolytes without the addition of external redox agents. This method relies on generating oxygen functional groups by inducing hydrolysis of water molecules within the gel electrolyte, which promotes functionalization of the graphitic electrodes, particularly at the defective sites of the as-prepared electrodes. This leads to the performance enhancement of quasi-solid-state supercapacitors made of graphitic electrodes and PVA+H_2SO_4 gel electrolyte. The redox reactions at the electrode/electrolyte interface arise from the elevated presence of oxygen functional groups on the electrode's surface. Also, we show that the oxygen functionalization simultaneously improves the double-layer contribution to the overall capacitance thanks to improved electrolyte intercalation of the graphitic electrodes. The functionalized cells exhibit a promising electrochemical performance with good cycling stability.

These insights indicate a simple path to significantly enhance the performance of supercapacitors using gel-based electrolytes, which are key to the fabrication of quasi-solid-state supercapacitors. This approach offers a new path to develop further miniaturized on-chip energy storage systems, which are compatible with silicon electronics and can support the power demand to operate integrated smart systems.

4. Experimental Section

4.1 Preparation of the electrodes

3C-SiC (cubic polytype) films, epitaxially grown on Si (100) substrates have been purchased from NOVASiC. The silicon carbide layers are ~500 nm thick and have been chemically and mechanically polished (StepSiC® by NOVASIC (France)) [56]. The graphitization of the SiC

films has been carried out using a solid-source approach mediated by a catalytic metal alloy [36-37]. The metal layers, either only a Ni or a combination of Ni and Cu, were sputtered on the 3C-SiC/Si(100) substrates using a Cryopump deposition chamber with CD Ar^+ ion and 200 mA current. The sputtering rates for Ni and Cu were ~ 0.05 nm/s and ~ 0.1 nm/s, respectively. The metal-coated substrates were annealed to ~1100 °C (25 °C /min) for an hour under vacuum condition (~10^{-5} mbar). The high-temperature annealing in the presence of the metallic layer promotes the breakage of Si-C bonds on the SiC surface to form Ni silicides. The released atomic C is then available to form graphene or graphitic carbon, depending on the selected catalytic layer and process. The remaining metal residues and reaction by-products were removed using a chemical wet etching for ~ 9 h (Freckle solution, for detailed information on this approach, refer to [36-37]).

Low-defect graphitic electrodes were synthesized by depositing a Ni layer (~10 nm) and a Cu layer (~ 20 nm) over the SiC surface, followed by an annealing process at 1100°C (**Figure 1a** and **g**). The use of a single thin Ni catalyst layer (~ 3 nm) leads to substantially more defective and oxidized graphene (**Figure 1h**). As the Ni layer is very thin, a significant amount of the catalyst film is transformed into nickel oxide upon exposure to air [57-58], leading to the synthesis of graphene with a high content of oxygen (oxidized electrodes). The electrodes were left intentionally exposed to air for at least 24 hours before the high-temperature annealing to promote the oxidation of nickel. Kenney et al. [58] report that the native nickel oxide thickness is limited to ~ 2 nm. Finally, in order to prepare a porous graphitic electrode, the single catalyst (Ni) procedure were repeated for a few cycles [39]. Here, we have employed two cycles of Ni deposition (~ 8 nm), annealing and Freckle wet etching, leading to a rough surface with open porosity (**Figure 1c** and **f**).

4.2 Fabrication of the quasi-solid-state supercapacitors

Quasi-solid-state supercapacitors were fabricated using a sandwich cell design (**Figure S1**). This design is based on using two electrodes (~2×1 cm^2) with a gel electrolyte in between the electrodes (the working area is ~0.9 cm^2) [19]. The cells were sealed with Kapton tape and stored for a few hours before testing. The typical thickness of the gel electrolyte used here is ~300 μm. The PVA+H_2SO_4 gel electrolyte was prepared by adding 3g PVA molecule (99 % purity and 108K molecular weight) to 30 mL deionized (DI) water followed by the addition of 3g of H_2SO_4 (98%) and stirring at 80 °C for a few hours to become completely transparent.

4.3 Characterization

The electrode surface was imaged using a Zeiss Supra 55VP scanning electron microscope (SEM) operating at 10 KeV and Dimension 3100 SPM atomic force microscope (AFM) by non-contact mode. The samples were cleaned using acetone, isopropanol, and de-ionized water before SEM and AFM measurements and were mounted on the sample holders using double-sided copper tape. SEM and AFM characterizations were conducted on the same electrodes used to fabricate the devices. EDS measurement was conducted using a Zeiss Supra 55VP SEM (10 KeV). Raman spectra were measured using a WiTec Raman microscope equipped with a green wavelength (532 nm) laser, by collecting maps over 100 μm^2 areas, made of 2500 single spectra. The Raman data reported is the average of the collected spectra from such maps. The FTIR measurements were conducted at room temperature using a Thermo Scientific Nicolet 6700 ATR-FTIR for the entire wavelength range (400 - 4000 cm^{-1}). The data was collected 64 times and the data reported here is the average spectra. The peak intensity was calculated based on the peak area. The FTIR data reported for the functionalized sample is collected on the cleaned

electrode after opening the cell. The electrodes were cleaned by sonication in de-ionized water until no electrolyte residue was observable.

4.4 Electrochemical characterization

The electrochemical performance of the supercapacitors was evaluated with an electrochemical workstation (CH Instruments, 660 E Model) in a two-probe configuration (**Figure S1 b**). Galvanostatic charge/discharge (CD) measurements were performed at room temperature with different currents: 1-5 μA with a potential window of 1 V. Data reported here are the averaged values calculated from 5 to 10 charge/discharge cycles. The CD test was used for assessing the supercapacitor's stability over 6000 cycles using 3 μA current and 1 V potential window. The areal specific capacitance of the electrodes (C) was calculated based on the CD data using equation 1 over the discharge period of the curve [14, 59]

$$C = 4I \times \frac{2\int V dt}{V^2|_{V_i}^{V_f}} \qquad (1)$$

where C is the areal specific capacitance of the electrodes in (μFcm^{-2}), I represent the current density (μAcm^{-2}), V is the CD potential (V), V_i and V_f are the initial and final voltages in the discharge cycle (V). $\int V dt$ represents the area under the CD discharge curve. The Coulombic efficiency of the supercapacitors was estimated by $100 \times \int V dt|_d / \int V\, dt|_c$, where d and c represent the discharge and charge periods.

Electrochemical Impedance Spectroscopy measurements were performed in a 0.01 Hz to 100 KHz frequency range with a signal amplitude of 5 mV.

The in-situ functionalization process was performed at room temperature by charging the cells with 1 or 3 μA current for ~10 minutes in a 2V potential window.

Corresponding Author

*E-mail: francesca.iacopi@uts.edu.au

Author Contributions

The manuscript was written through the contributions of all authors. All authors have given approval to the final version of the manuscript.

Funding Sources

Air Force Office for Scientific Research (grant 18IOA052).

Acknowledgments

The authors kindly acknowledge funding from the Air Force Office for Scientific Research through the Asian Office for Aerospace Research and Development (AOARD, grant 18IOA052). The authors wish to thank Dr. Neeraj Mishra and Mr. Geoff McCredie for their kind support and assistance throughout this work. The UTS MAU labs are acknowledged for providing access to the fabrication facilities.

References

[1] J. Liang, A. K. Mondal, D.-W. Wang, F. Iacopi, *Adv. Mater. Technol.* **2019**, *4*, 1800200.
[2] C. Liu, F. Li, L. P. Ma, H. M. Cheng, *Adv. Mater.* **2010**, *22*, E28-E62.
[3] Z. Niu, L. Zhang, L. Liu, B. Zhu, H. Dong, X. Chen, *Adv. Mater.* **2013**, *25*, 4035-4042.
[4] C.-H. Chang, B. Hsia, J. P. Alper, S. Wang, L. E. Luna, C. Carraro, S.-Y. Lu, R. Maboudian, *ACS Appl. Mater. Interfaces* **2015**, *7*, 26658-26665.

[5] J. Li, S. Sollami Delekta, P. Zhang, S. Yang, M. R. Lohe, X. Zhuang, X. Feng, M. Östling, *ACS Nano* **2017**, *11*, 8249-8256.

[6] W. Hooch Antink, Y. Choi, K. d. Seong, J. M. Kim, Y. Piao, *Adv. Mater. Interfaces* **2018**, *5*, 1701212.

[7] E. Frackowiak, F. Beguin, *Carbon* **2001**, *39*, 937-950.

[8] M. Conte, *Fuel Cells* **2010**, *10*, 806-818.

[9] J. R. Miller, R. Outlaw, B. Holloway, *Science* **2010**, *329*, 1637-1639.

[10] M. Toupin, T. Brousse, D. Bélanger, *Chem. Mater.* **2004**, *16*, 3184-3190.

[11] G. Ma, M. Dong, K. Sun, E. Feng, H. Peng, Z. Lei, *J. Mater. Chem. A* **2015**, *3*, 4035-4041.

[12] Y. Xu, Z. Lin, X. Huang, Y. Wang, Y. Huang, X. Duan, *Adv. Mater.* **2013**, *25*, 5779-5784.

[13] Y. Fang, B. Luo, Y. Jia, X. Li, B. Wang, Q. Song, F. Kang, L. Zhi, *Adv. Mater.* **2012**, *24*, 6348-6355.

[14] L.-Q. Fan, Q.-M. Tu, C.-L. Geng, J.-L. Huang, Y. Gu, J.-M. Lin, Y.-F. Huang, J.-H. Wu, *Electrochim. Acta* **2020**, *331*, 135425.

[15] L. Wang, Z. Sofer, M. Pumera, *ACS Nano* **2020**.

[16] H. Yu, J. Wu, L. Fan, K. Xu, X. Zhong, Y. Lin, J. Lin, *Electrochim. Acta* **2011**, *56*, 6881-6886.

[17] H. Yu, J. Wu, L. Fan, Y. Lin, K. Xu, Z. Tang, C. Cheng, S. Tang, J. Lin, M. Huang, *J. Power Sources* **2012**, *198*, 402-407.

[18] B. Aljafari, T. Alamro, M. K. Ram, A. Takshi, *J. Solid State Electrochem.* **2018**, 1-9.

[19] B. Wang, M. Ahmed, B. Wood, F. Iacopi, *Appl. Phys. Lett.* **2016**, *108*, 183903.

[20] Y. Xu, Z. Lin, X. Huang, Y. Liu, Y. Huang, X. Duan, *ACS Nano* **2013**, *7*, 4042-4049.

[21] B. Karaman, A. Bozkurt, *Int. J. Hydrogen Energy* **2018**, *43*, 6229-6237.

[22] C. Zhong, Y. Deng, W. Hu, J. Qiao, L. Zhang, J. Zhang, *Chem. Soc. Rev.* **2015**, *44*, 7484-7539.

[23] Y. Zhao, J. Liu, B. Wang, J. Sha, Y. Li, D. Zheng, M. Amjadipour, J. MacLeod, N. Motta, *ACS Appl. Mater. Interfaces* **2017**, *9*, 22588-22596.

[24] M. S. Kim, B. Hsia, C. Carraro, R. Maboudian, *Carbon* **2014**, *74*, 163-169.

[25] Y. Liang, W. Zhang, D. Wu, Q. Q. Ni, M. Q. Zhang, *Adv. Mater. Interfaces* **2018**, *5*, 1800430.

[26] L.-Q. Fan, G.-J. Liu, C.-Y. Zhang, J.-H. Wu, Y.-L. Wei, *Int. J. Hydrogen Energy* **2015**, *40*, 10150-10157.

[27] B. Wang, J. Liu, Y. Zhao, Y. Li, W. Xian, M. Amjadipour, J. MacLeod, N. Motta, *ACS Appl. Mater. Interfaces* **2016**, *8*, 22316-22323.

[28] A. Ouerghi, M. Marangolo, R. Belkhou, S. El Moussaoui, M. Silly, M. Eddrief, L. Largeau, M. Portail, B. Fain, F. Sirotti, *Phys. Rev. B* **2010**, *82*, 125445.

[29] M. Amjadipour, A. Tadich, J. J. Boeckl, J. Lipton-Duffin, J. MacLeod, F. Iacopi, N. Motta, *Nanotechnology* **2018**, *29*, 145601.

[30] N. Mishra, J. Boeckl, N. Motta, F. Iacopi, *Phys. Status Solidi (a)* **2016**, *213*, 2277-2289.

[31] C. Riedl, C. Coletti, U. Starke, *J. Phys. D: Appl. Phys.* **2010**, *43*, 374009.

[32] W. A. De Heer, C. Berger, M. Ruan, M. Sprinkle, X. Li, Y. Hu, B. Zhang, J. Hankinson, E. Conrad, *Proc. Natl. Acad. Sci.* **2011**, *108*, 16900-16905.

[33] S. Wang, B. Hsia, C. Carraro, R. Maboudian, *J. Mater. Chem. A* **2014**, *2*, 7997-8002.

[34] F. Liu, A. Gutes, I. Laboriante, C. Carraro, R. Maboudian, *Appl. Phys. Lett.* **2011**, *99*, 112104.

[35] B. Hsia, M. S. Kim, M. Vincent, C. Carraro, R. Maboudian, *Carbon* **2013**, *57*, 395-400.

[36] F. Iacopi, N. Mishra, B. V. Cunning, D. Goding, S. Dimitrijev, R. Brock, R. H. Dauskardt, B. Wood, J. Boeckl, *J. Mater. Res.* **2015**, *30*, 609-616.

[37] N. Mishra, J. J. Boeckl, A. Tadich, R. T. Jones, P. J. Pigram, M. Edmonds, M. S. Fuhrer, B. M. Nichols, F. Iacopi, *J. Phys. D: Appl. Phys.* **2017**, *50*, 095302.

[38] B. V. Cunning, M. Ahmed, N. Mishra, A. R. Kermany, B. Wood, F. Iacopi, *Nanotechnology* **2014**, *25*, 325301.

[39] M. Ahmed, B. Wang, B. Gupta, J. J. Boeckl, N. Motta, F. Iacopi, *J. Electrochem. Soc.* **2017**, *164*, A638-A644.

[40] L. Malard, M. Pimenta, G. Dresselhaus, M. Dresselhaus, *Phys. Rep.* **2009**, *473*, 51-87.

[41] A. C. Ferrari, *Solid State Commun.* **2007**, *143*, 47-57.

[42] F. Iacopi, G. Walker, L. Wang, L. Malesys, S. Ma, B. V. Cunning, A. Iacopi, *Appl. Phys. Lett.* **2013**, *102*, 011908.

[43] B. Gupta, M. Notarianni, N. Mishra, M. Shafiei, F. Iacopi, N. Motta, *Carbon* **2014**, *68*, 563-572.

[44] M. P. Araújo, O. Soares, A. Fernandes, M. Pereira, C. Freire, *RSC Adv.* **2017**, *7*, 14290-14301.

[45] S. A. You, O. S. Kwon, J. Jang, *J. Mater. Chem.* **2012**, *22*, 17805-17812.

[46] K. S. Kim, Y. M. Um, J.-r. Jang, W.-S. Choe, P. J. Yoo, *ACS Appl. Mater. Interfaces* **2013**, *5*, 3591-3598.

[47] A. Joshi, A. Bajaj, R. Singh, P. Alegaonkar, K. Balasubramanian, S. Datar, *Nanotechnology* **2013**, *24*, 455705.

[48] Z. Li, R. J. Young, I. A. Kinloch, *ACS Appl. Mater. Interfaces* **2013**, *5*, 456-463.

[49] N. Mishra, M. Bosi, F. Rossi, G. Salviati, J. Boeckl, F. Iacopi, *J. Appl. Phys.* **2019**, *126*, 065304.

[50] K. Haubner, J. Murawski, P. Olk, L. M. Eng, C. Ziegler, B. Adolphi, E. Jaehne, *ChemPhysChem* **2010**, *11*, 2131-2139.

[51] Q. Pan, N. Tong, N. He, Y. Liu, E. Shim, B. Pourdeyhimi, W. Gao, *ACS Appl. Mater. Interfaces* **2018**, *10*, 7927-7934.

[52] S. Sarkar, K. Raul, S. Pradhan, S. Basu, A. Nayak, *Phys. E* **2014**, *64*, 78-82.

[53] N. Ghaderi, M. Peressi, *J. Phys. Chem. C* **2010**, *114*, 21625-21630.

[54] S. Tang, S. Zhang, *Chem. Phys.* **2012**, *392*, 33-45.

[55] H. C. Schniepp, J.-L. Li, M. J. McAllister, H. Sai, M. Herrera-Alonso, D. H. Adamson, R. K. Prud'homme, R. Car, D. A. Saville, I. A. Aksay, *J. Phys. Chem. B* **2006**, *110*, 8535-8539.

[56] B. Gupta, I. Di Bernardo, P. Mondelli, A. Della Pia, M. G. Betti, F. Iacopi, C. Mariani, N. Motta, *Nanotechnology* **2016**, *27*, 185601.

[57] S. Oswald, W. Brückner, *Surf. Interface Anal.* **2004**, *36*, 17-22.

[58] M. J. Kenney, M. Gong, Y. Li, J. Z. Wu, J. Feng, M. Lanza, H. Dai, *Science* **2013**, *342*, 836-840.

[59] S. Roldán, D. Barreda, M. Granda, R. Menéndez, R. Santamaría, C. Blanco, *Phys. Chem. Chem. Phys.* **2015**, *17*, 1084-1092.